A Feedback Controlled MEMS Nanopositioner for On-Chip High-Speed AFM

Ali Mohammadi, *Student Member, IEEE*, Anthony G. Fowler, *Student Member, IEEE*, Yuen K. Yong, *Member, IEEE*, and S. O. Reza Moheimani, *Fellow, IEEE*

***Abstract*— We report the design of a two-degree-of-freedom microelectromechanical systems nanopositioner for on-chip atomic force microscopy (AFM). The device is fabricated using a silicon-on-insulator-based process to function as the scanning stage of a miniaturized AFM. It is a highly resonant system with its lateral resonance frequency at ∼850 Hz. The incorporated electrostatic actuators achieve a travel range of 16 μm in each direction. Lateral displacements of the scan table are measured using a pair of electrothermal position sensors. These sensors are used, together with a positive position feedback controller, in a feedback loop, to damp the highly resonant dynamics of the stage. The feedback controlled nanopositioner is used, successfully, to generate high-quality AFM images at scan rates as fast as 100 Hz. [2013-0063]**

***Index Terms*— Nanopositioning, MEMS, electrothermal sensor, on-chip, AFM.**

I. Introduction

A NANOPOSITIONER is a mechanical device that is capable of producing repeatable, high-precision motion with nanometer resolution. This is an invaluable quality in many areas of micro and nanotechnology, with this type of motion commonly being required by processes that involve the positioning, manipulation and interrogation of samples in a range of micro-scale applications, including molecular biology, nanoassembly, and optical alignment systems [1]–[4].

There has recently been increasing interest in the development of novel nanopositioning devices that are based on microelectromechanical systems (MEMS) fabrication processes [5]–[8]. These miniaturized nanopositioners potentially hold a number of advantages over conventional macro-sized nanopositioners. Characteristics such as increased operating bandwidths, lower unit manufacturing costs, simpler bulk fabrication and a much smaller packaged size [5], [9] mean that MEMS-based nanopositioners represent an attractive solution for many applications. These attributes have been exploited in recent high-density probe-based data storage devices, in which MEMS nanopositioners are featured as a fundamental component of the system [10]–[12].

Recent MEMS nanopositioners have also implemented feedback control techniques to improve the static and dynamic performance of the fabricated system. As shown in [13], [14] a closed-loop control system can be used to achieve a higher positioning accuracy and alleviate imperfections inherent in the microactuator such as drift and vibrations.

One of the most important tools used in science and engineering in recent times is the atomic force microscope (AFM) [15]. The AFM features a sharp probe of a few nanometers wide, and is used to interrogate sample surfaces down to the atomic scale. The use of a MEMS-based nanopositioner as the scanning stage of an AFM greatly reduces the size of one of the main components of the system. This represents an important step towards the development of miniaturized, mass-produced AFMs that represent a fully-integrated, low-cost solution for on-chip scanning. Such a MEMS-based AFM scanner was demonstrated in [16], where a 2-degree-of-freedom (DOF) MEMS nanopositioner fabricated using a commercial silicon-on-insulator (SOI) process was used in place of the existing scanning stage for an off-the-shelf AFM. The nanopositioner's stage contained a series of 3 μm gold features that were used to represent a scan sample, and an open-loop scan of the features was successfully performed by the AFM in tapping mode.

This paper extends the previous results reported in [16] by introducing an enhanced version of the MEMS nanopositioner that features integrated displacement sensors which measure the motions of the stage along each of its two axes. The use of standard MEMS fabrication processes means that it is relatively straightforward to integrate these sensors into the existing system without the need for additional complex manufacturing steps. By adding displacement sensors to the nanopositioning system, the device can be integrated in a closed-loop control system to improve the static and dynamic performance of the nanopositioner, enhancing its performance during use as an AFM scanning stage. A schematic representation of a 1-DOF nanopositioner is shown in Fig. 1, demonstrating how stage displacement measurements made by the electrothermal sensors can be utilized for closed-loop control of the system.

The remainder of this paper continues as follows. Sec. II describes the design of the MEMS scanner and its modal analysis result. The electrothermal sensor design and the readout circuit are presented in Sec. III. The characterization

Manuscript received March 6, 2013; revised June 20, 2013; accepted October 7, 2013. Date of publication December 5, 2013; date of current version May 29, 2014. This work was supported in part by the Australian Research Council and in part by The University of Newcastle. Subject Editor A. M. Shkel.

The authors are with the School of Electrical Engineering and Computer Science, The University of Newcastle, Callaghan, N.S.W. 2308, Australia (e-mail: mohamadi@ieee.org; anthony.fowler@uon.edu.au; yuenkuan.yong@newcastle.edu.au; reza.moheimani@newcastle.edu.au).

Color versions of one or more of the figures in this paper are available online at http://ieeexplore.ieee.org.

Digital Object Identifier 10.1109/JMEMS.2013.2287506

1057-7157 © 2013 IEEE. Personal use is permitted, but republication/redistribution requires IEEE permission.
See http://www.ieee.org/publications_standards/publications/rights/index.html for more information.

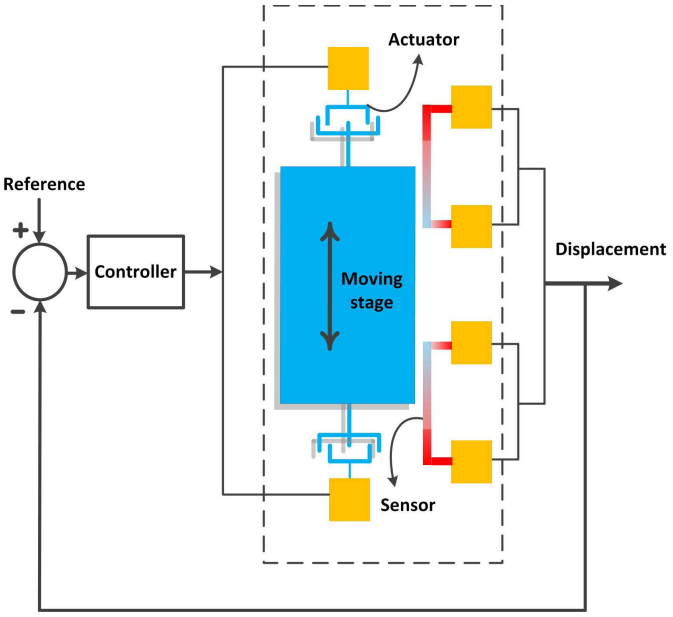

Fig. 1. A schematic diagram of a 1-DOF nanopositioner with electrostatic actuators and electrothermal sensors in a closed-loop control system.

of the device, which includes sensor sensitivity and frequency response measurements, and static non-linearity linearization of the nanopositioner, is discussed in Sec. IV. Sec. V presents the design and implementation of controllers to suppress resonant modes of the device and to facilitate good tracking of reference signals. Sec. VI evaluates the performance of the MEMS nanopositioner for AFM imaging. Sec. VII concludes the paper.

II. MEMS Scanner Design

The MEMS nanopositioner featured in this paper is an evolution of the device described and tested in [16], and is fabricated using a commercial SOI MEMS process. As previously stated, the design has been modified such that the nanopositioner features integrated electrothermal sensors that enable real-time measurements of the stage displacement along the x and y directions. The fabricated nanopositioner is shown in Fig. 2.

The scanner has two mechanical degrees of freedom, with electrostatic comb-finger actuators being used to position a 3 mm × 3 mm stage along the planar x and y directions. The mechanical design of the nanopositioner is based on a parallel-kinematic configuration, with a series of beam flexures around the perimeter of the stage being used to position the stage along the x and y axes, and also to decouple the motions of the two axes. To prevent damage occurring to the electrostatic actuators due the application of excessively high actuation voltages, mechanical stoppers are used to physically limit the displacement of the stage along each axis to 20 μm.

Each of the nanopostioner's electrostatic actuators feature interdigitated comb fingers with a width of 2 μm, and with a spacing of 2 μm between adjacent fingers. These are chosen according to the minimum dimensions permitted by the fabrication process in order to maximize the force generated by the actuator for a given actuation voltage.

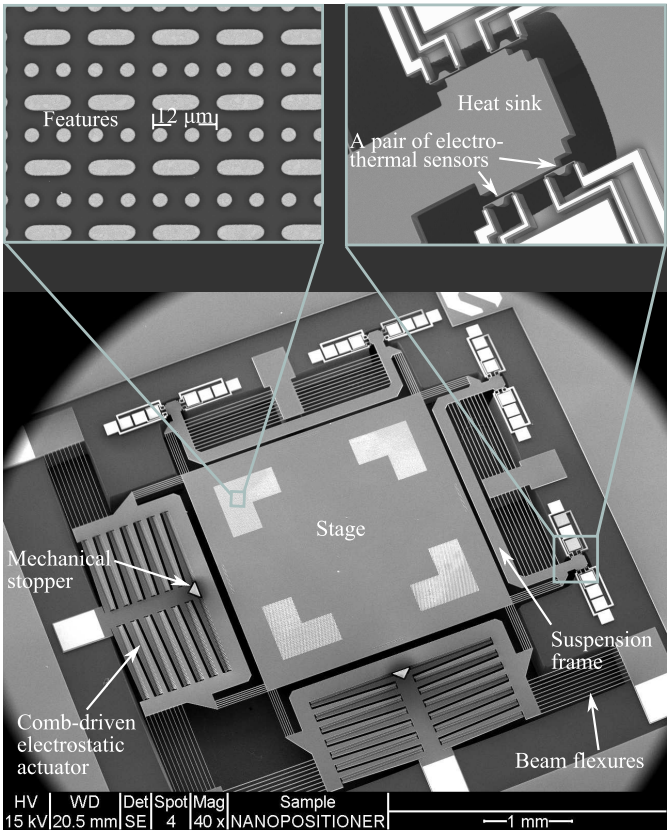

Fig. 2. SEM images of fabricated 2-DOF nanopositioner, showing electrothermal sensors and integrated gold features.

This allows the stiffness of the beam flexures to be increased, resulting in the nanopositioner having higher in-plane resonance frequencies while maintaining a useful actuation range. The ratio between the beam height and width (approximately 7:1) means that the z axis stiffness is higher than the in-plane stiffness, which is a desired quality for AFM applications [17].

As part of the design process, the MEMS design software package CoventorWare was used to perform a modal analysis of the system. As shown in the simulation results in Fig. 3, the nanopositioner's first in-plane resonant mode is located at approximately 903 Hz. The mechanical symmetry of the device means that this mode exists for both of the device's in-plane axes.

The MEMS nanopositioner was fabricated via MEMSCAP's commercial silicon-on-insulator SOIMUMPs process [18]. The main device layer is comprised of 25 μm-thick doped silicon, and contains the major structures of the device including the actuators, displacement sensors, stage, and flexures.

III. Position Sensors for the 2-DOF Nanopositioner

A. The Electrothermal Displacement Sensor

Displacement sensing technologies available in MEMS devices are based on capacitive [19], piezoresistive [20], and electrothermal [21] effects. Fabrication of the capacitive

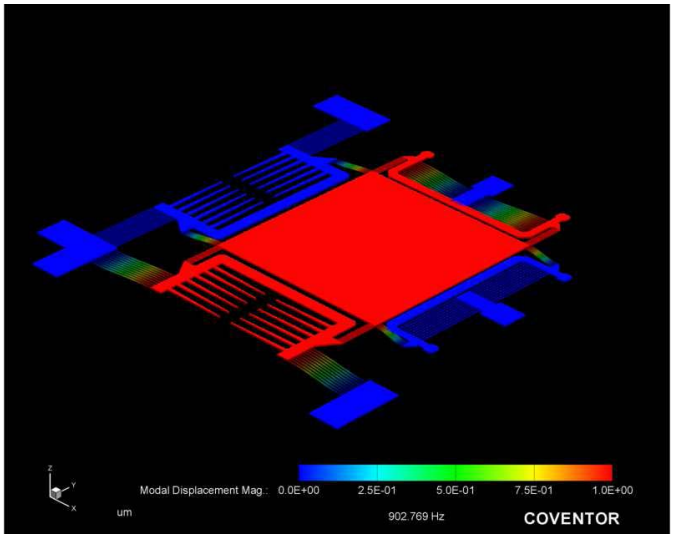

Fig. 3. Simulated first in-plane resonant mode of nanopositioner.

sensors is highly compatible with standard MEMS fabrication processes. However, piezoresistive and electrothermal sensors can be fabricated with much smaller footprints, which makes them rather attractive in applications where space is at a premium. These sensors map displacements of a stage to variations in the resistivity of a transducer, typically made of doped silicon. Piezoresistive sensors can be operated at lower power levels compared to electrothermal sensors. However, the resistance of the doped silicon is more sensitive to temperature changes than variations in mechanical stress [22]. The small footprint and high sensitivity of electrothermal sensors were our motivation to utilize this technology to measure displacements of the nanopositioning stage.

An early implementation of the electrothermal displacement sensor was reported in [21], and it was subsequently used in a probe-based data storage device reported in [10]. The operating principle of the sensor is based on utilizing the temperature sensitivity of doped silicon resistance. The conduction of electrical power through the doped silicon increases its temperature. The transfer of heat between a moving heat sink (the nanopositioner stage in this case) and a stationary hot resistor (sensor) changes the sensor resistance, as depicted in the 1-DOF nanopositioner schematic in Fig. 1, where the stage is actuated electrostatically. The narrow spacing between the heat sink and the sensor results in the heat transfer mechanism being dominated by conduction [23]. As the stage moves, it absorbs heat from the resistor. When the resistor temperature changes its resistivity will change. Therefore, voltages derived from the change of the sensor's resistivity are highly correlated with displacement, and can be used to represent the displacement of the stage.

The nanopositioner's electrothermal sensors are arranged in a differential topology, in order to improve the sensor linearity and reject common mode signals. In previously reported electrothermal sensing implementations, the heaters have typically featured a uniform cross section [9], [21], [23]. Here, the integrated sensors are designed to have a nonuniform profile. As discussed in [24], electrothermal heaters with this shape display a flatter spatial temperature distribution that leads to higher sensor linearity and sensitivity. Further analysis of the sensor design and characteristics including drift and bandwidth are also presented in [24].

B. Proposed Structure for the Integrated Sensor

The use of electrothermal sensors in 1-DOF nanopositioners has been reported in recent literature, e.g. see [23], [25]. In such designs the distance between the sensor and the stage must be kept fixed in order to make precise measurements of the lateral movements of the stage. It is rather difficult to achieve this objective in a 2-DOF planar design [19]. Here, we exploit the unique structure of the 2-DOF nanopositioner, described in Sec. II, to incorporate the electrothermal displacement sensors for both axes. A scanning electron microscope (SEM) micrograph of the proposed 2-DOF nanopositioner with integrated electrothermal displacement sensors is shown in Fig. 2. The frames have elongated ends, compared to our previous design reported in [16], in order to accommodate the addition of the electrothermal sensors. The decoupled mechanical design facilitates independent motions of the frames along the two lateral axes. Thus, the frame that tracks the stage displacement in one direction is fixed in the orthogonal direction. Hence, the lateral motions of the stage are followed by the frames independently, which leads to a fixed gap between each sensor and its corresponding frame.

The length of each sensor is $50\,\mu$m, which is sufficient for measuring the full travel range of the stage. The sensors were designed to have resistance values of approximately $200\,\Omega$. In the fabricated nanopositioner, however, the sensor resistances vary from $160\,\Omega$ to $300\,\Omega$. The offset voltages generated by these differences can be corrected through the use of potentiometers in the readout circuitry. The sensor resistance variations may still result in varying sensitivities between the sensors. However, these variations are addressed through the use of look-up tables, as articulated in Sec. IV.

C. Readout Circuitry

As stated earlier, the desired sensor output is the heater resistivity changes, which are highly correlated with the movements of the stage. Common readout circuits for resistive measurements are based on techniques involving RC-decay, oscillator frequency, resistance-to-current conversion and resistance-to-voltage conversion [26]. In the first approach, a voltage pulse is applied to the RC circuit, and the time it takes for the output voltage to reach to a certain threshold can be measured from the variation in resistance or capacitance [27]. This method is effective for resistive sensors that have a large dynamic range. The resistivity change in an electrothermal sensor, however, is typically less than 10% of its nominal value, which does not lead to a significant RC variation. The effectiveness of the second approach is impeded by the phase noise of the oscillator. Particularly, if a ring oscillator is used, it is known that the phase noise contributes substantially to the total measurement noise and reduces the achievable SNR [28].

To avoid these complications, we chose to design the readout circuit based on the concept of resistance-to-voltage

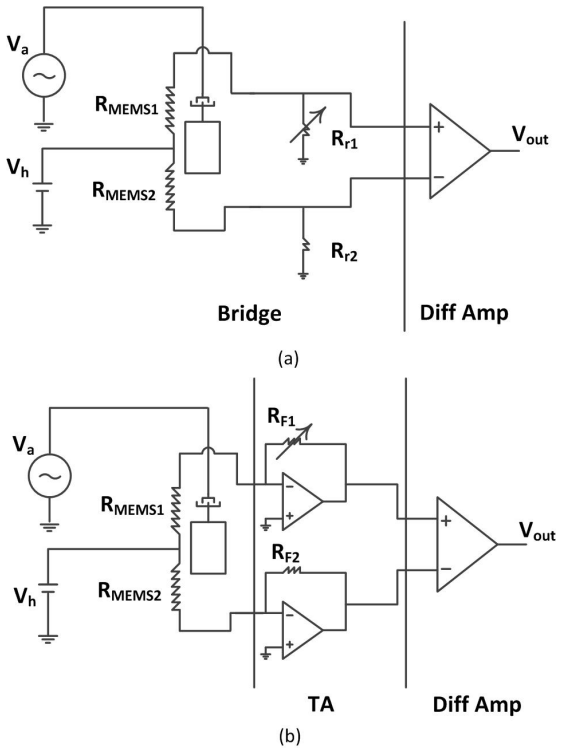

Fig. 4. Readout circuit schematics: a) Wheatstone bridge. b) TA.

conversion, which uses a Wheatstone bridge, and resistance-to-current conversion, which uses transimpedance amplifiers (TA). Both methods were implemented and tested on the MEMS nanopositioner. The Wheatstone bridge is commonly used in resistive readout circuits. However, it turns out that for identical resistive changes, a TA-based read out circuit offers a higher sensitivity.

The readout circuits corresponding to the two methods are schematically illustrated in Fig. 4. The actuation voltage, represented by V_a, drives the electrostatic actuator. V_h is the dc heating voltage, $R_{MEMS1,2}$ are the sensor heated resistors and $R_{r1,2}$, $R_{F1,2}$ are the bridge reference and the TA feedback resistors, respectively. The sensor resistance variations can be described as

$$R_{MEMS1,2} = R \pm \delta R, \tag{1}$$

where R is the MEMS resistor value with the stage at the middle (no displacement) and δR is the resistance changes associated with the stage displacement. Assuming that $R_{r1} = R_{r2} = R_{ref}$, the bridge output voltage is

$$V_{outB} = A\frac{2R_{ref}\delta R}{(R + R_{ref})^2}V_h, \tag{2}$$

where A is the differential amplifier voltage gain and V_h is the bias voltage, which heats the sensors. The balanced bridge conditions lead to $R = R_{r1,2}$. Therefore, the total gain can be obtained as

$$\frac{V_{outB}}{\delta R} = \frac{AV_h}{2R}. \tag{3}$$

Similarly, the output voltage for the TA circuit is given by

$$V_{outT} = A\frac{2R_F\delta R}{(R^2 - \delta R^2)}V_h \tag{4}$$

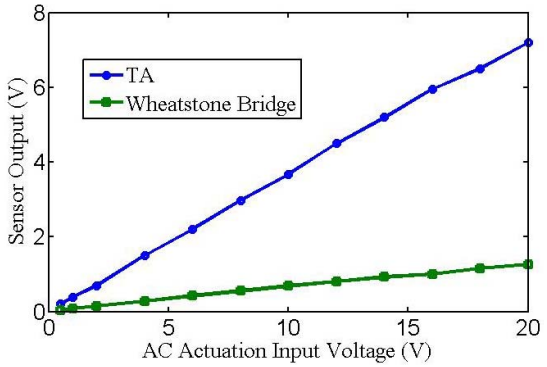

Fig. 5. Comparison of bridge and TA sensitivity.

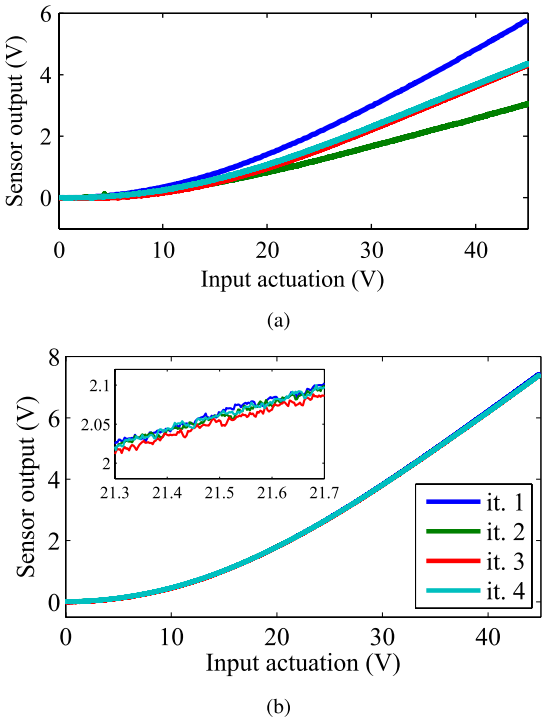

Fig. 6. Sensor sensitivity curves achieved by the same setup over four iterations using (a) the Wheatstone bridge and (b) the TA circuit.

As long as no voltage gain is expected from the TA, we may assume $R = R_{F1,2}$. Therefore, neglecting δR^2, the total gain can be approximated as:

$$\frac{V_{outT}}{\delta R} = \frac{2AV_h}{R} \tag{5}$$

Comparing Eqs. (3) and (5) we note that the achievable sensitivity with the TA readout circuit is four times higher than with the bridge circuit. This is supported by experimental results, illustrated in Fig. 5, where for the same actuation voltage, a larger output voltage is obtained with the TA circuit. In particular, we note from this figure that the slope of the TA readout circuit transfer characteristic, i.e. its sensitivity, is much larger than that of the bridge circuit. Additionally, in the TA topology the heating voltage across the resistor is kept fixed, which leads to a constant voltage mode operation. In contrast, the bridge topology does not guarantee a constant voltage across the resistor. The curves shown in Fig. 6(a) are four iterations of the same measurement using the

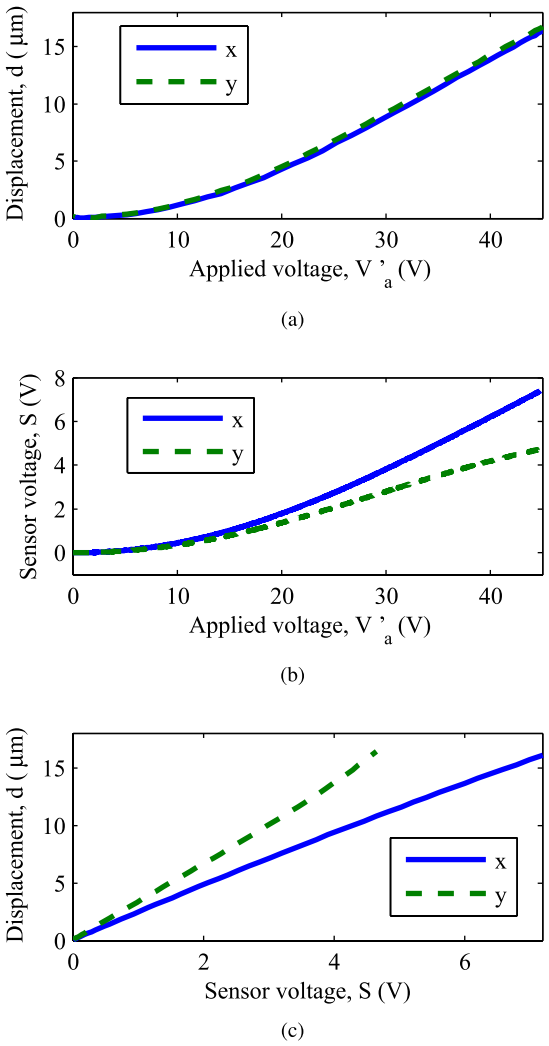

Fig. 7. Sensitivity measurement for x and y sensors. a) Stage displacement vs. input actuation voltage. b) Sensor output voltage vs. input actuation voltage. c) Sensor characteristic curve.

bridge circuit on one sensor, which indicate that a repeatable measurement cannot be ensured. The constant voltage mode operation achieved by the TA leads to similar outputs for the four iterations as demonstrated in Fig. 6(b).

IV. Device Characterization

A. Sensor Sensitivity Measurement

A Polytec PMA-400 Planar Motion Analyzer was used to measure the x and y displacements of the nanopositioner. The measurements were based on the principle of stroboscopic video microscopy performed by in-built image analysis software of the PMA. Actuation voltages from 0 V to 45 V were applied to drive the x and y comb finger actuators, and the corresponding displacements (measured by the PMA) and sensor output voltages were recorded simultaneously. Results are plotted in Fig. 7. The nonlinearities shown in these plots are due to the nonlinear relationship between the generated force and the voltage applied to the comb actuators. With a maximum actuation voltage of 45 V, the measured displacement is 16 μm for both x and y axes. From the measured displacement versus sensor output plots shown in Fig. 7(c), the mean sensitivity of the x and y sensors were estimated from the slopes of linear best-fit curves fitted to the data. The mean sensitivity of the x and y sensors are approximately 2.29 μm/V and 3.42 μm/V respectively.

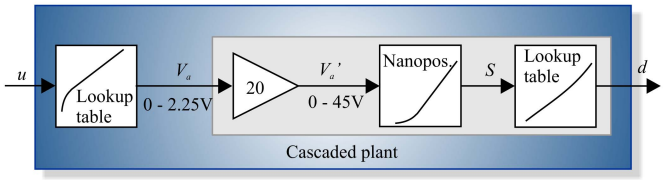

Fig. 8. Compensation for static nonlinearity using lookup tables.

The power spectral density (PSD) of the sensor output was measured by a HP35670A signal analyzer in order to determine the sensor resolution. The noise floor for the x-axis sensor (worst case) is -90 dBVrms/$\sqrt{Hz}$. In the open-loop actuator-sensor system this typically translates to a 1 nm displacement resolution over a 100 Hz frequency bandwidth.

B. Linearization of the Static Nonlinearity

The nonlinear relationship between input actuation voltage and actuator displacement resembles a high-order polynomial function. To linearize this, a lookup table was implemented in dSPACE and placed in series with the plant, as shown in Fig. 8. The lookup table stores the displacement data and actuation voltages of the MEMS nanopositioner. These stored values were obtained from the data plotted in Fig. 7(a). For every pre-defined input displacement u (in μm), the lookup table generates an output voltage V_a by interpolating/extrapolating among the stored values. The generated signal V_a was fed to a voltage amplifier which has a gain of 20. The output voltage of the amplifier is in turn used to drive the nanopositioner.

The sensors exhibit minor nonlinearities, which may be attributed to device imperfections due to tolerances in the MEMS fabrication process. These nonlinearities were linearized using a second lookup table (see Fig. 8) which stores the data plotted in Fig. 7(c). Similar to the first lookup table, for every sensor voltage S (in Volt) fed to the lookup table, the lookup table generates an output displacement d (in μm). By cascading the lookup tables with the plant, the input-output relationship from u to d was linearized.

C. Frequency Response Measurement

The x and y axes frequency response functions (FRFs) of the MEMS nanopositioner were obtained using the signal analyzer. Displacements of both the axes were biased to their mid-range which were at 8 μm. FRFs were recorded from the inputs applied to the cascaded plant u_x, u_y in Fig. 8 to the measured displacement d_x, d_y respectively.

Fig. 9 plots the experimentally determined open-loop FRFs for both the x and y axes. The first resonance frequency of the x axis is located at 860 Hz. For the y axis, the resonant peak appears at 850 Hz. These measured resonances are close to the ConventorWare simulated values. The dynamic range of the x and y resonant peaks are respectively 36.6 dB and 37.5 dB.

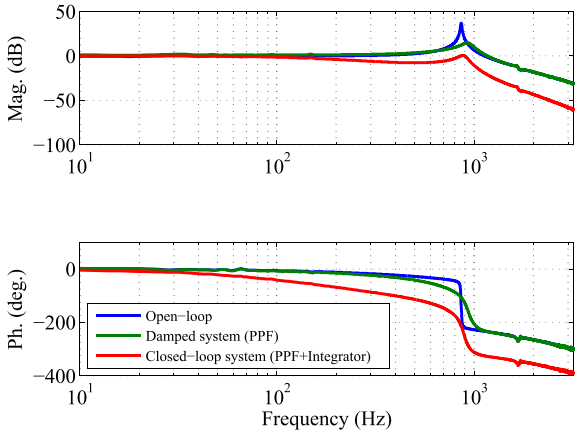

(a)

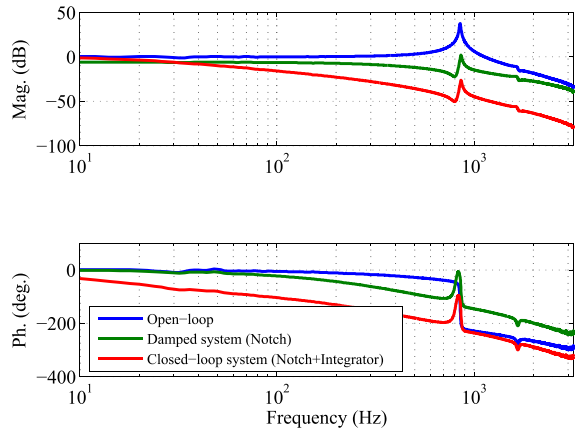

(b)

Fig. 9. Measured open- and closed-loop frequency responses of the (a) x, and (b) y axes.

V. Control Design and Implementation

The measured motion coupling from x-to-y and y-to-x are −40.7 dB (0.92%) and −42.5 dB (0.75%) respectively, which are remarkably low. Thus, the MEMS nanopositioner can be, effectively, considered as two single-input single-output (SISO) systems. A second-order model was fitted to the measured frequency response of each axis using the frequency-domain subspace algorithm [29]. The following are the two identified transfer functions of the SISO systems.

$$G_{d_x u_x} = \frac{0.1769s^2 - 2954s + 2.235 \times 10^7}{s^2 + 57.21s + 2.925 \times 10^7} \quad (6)$$

$$G_{d_y u_y} = \frac{0.1841s^2 - 3151s + 2.314 \times 10^7}{s^2 + 56.1s + 2.85 \times 10^7} \quad (7)$$

Next, a positive position feedback (PPF) controller was designed and implemented on the fast axis (x axis) of the nanopositioner to suppress its first resonance frequency. PPF, proposed by Caughey and coauthors [30], [31], is known to be an effective controller capable of providing substantial damping to collocated structures [32]. The transfer function of a PPF controller rolls-off at 40 dB/decade at high frequencies,

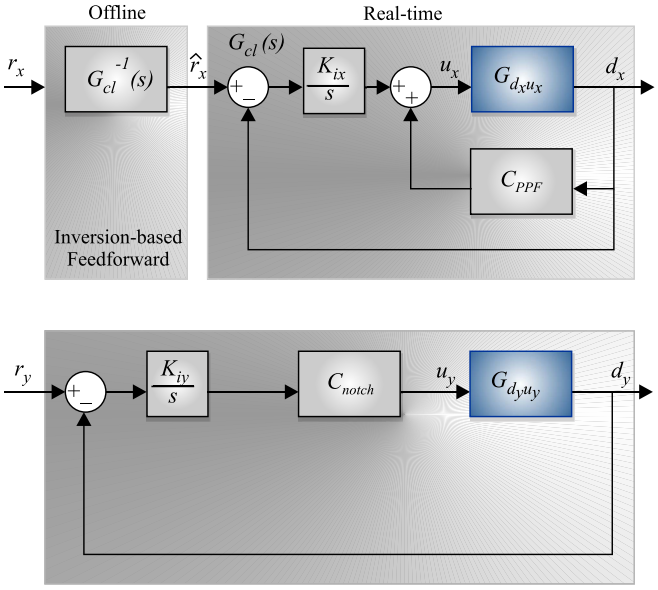

Fig. 10. Block diagram of control structures for the x and y axes.

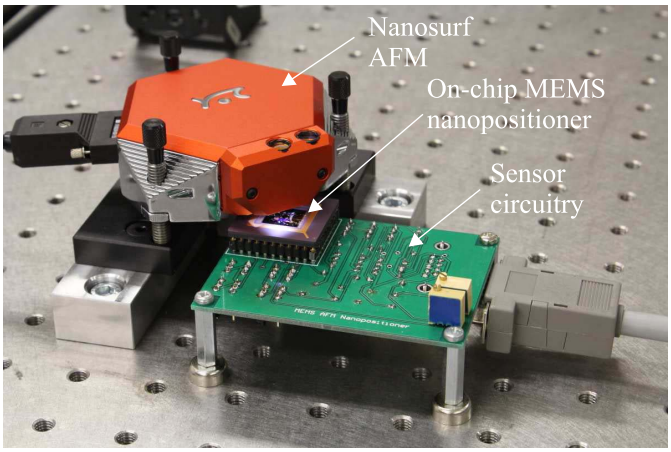

Fig. 11. Experimental setup of the AFM and MEMS nanopositioner in a scan-by-sample mode.

which is a desirable property to avoid the excitation of high frequency dynamics of the nanopositioner. An integral tracking controller was implemented in the outer loop to improve low frequency tracking (see Fig. 10). The combined control strategy is known to reduce crosstalk between the two lateral axes [33]. In a typical rastering application, the y axis is used to track a slow ramp set-point. Hence, the closed-loop bandwidth requirement on this axis is less demanding. A notch filter combined with an integral tracking controller [34] was designed and implemented on the y axis as shown in Fig. 10. Transfer functions of the two controllers are described in Eqs. (8) and (9) below.

$$C_{PPF} = \frac{5.5 \times 10^6}{s^2 + 4161s + 3.533 \times 10^7} \quad (8)$$

$$C_{notch} = \frac{s^2 + 289.9s + 2.574 \times 10^7}{s^2 + 2.899 \times 10^4 s + 2.574 \times 10^7} \quad (9)$$

A dSPACE-1103 rapid prototyping system, working at a sampling rate of 80 kHz, was used to implement the controller.

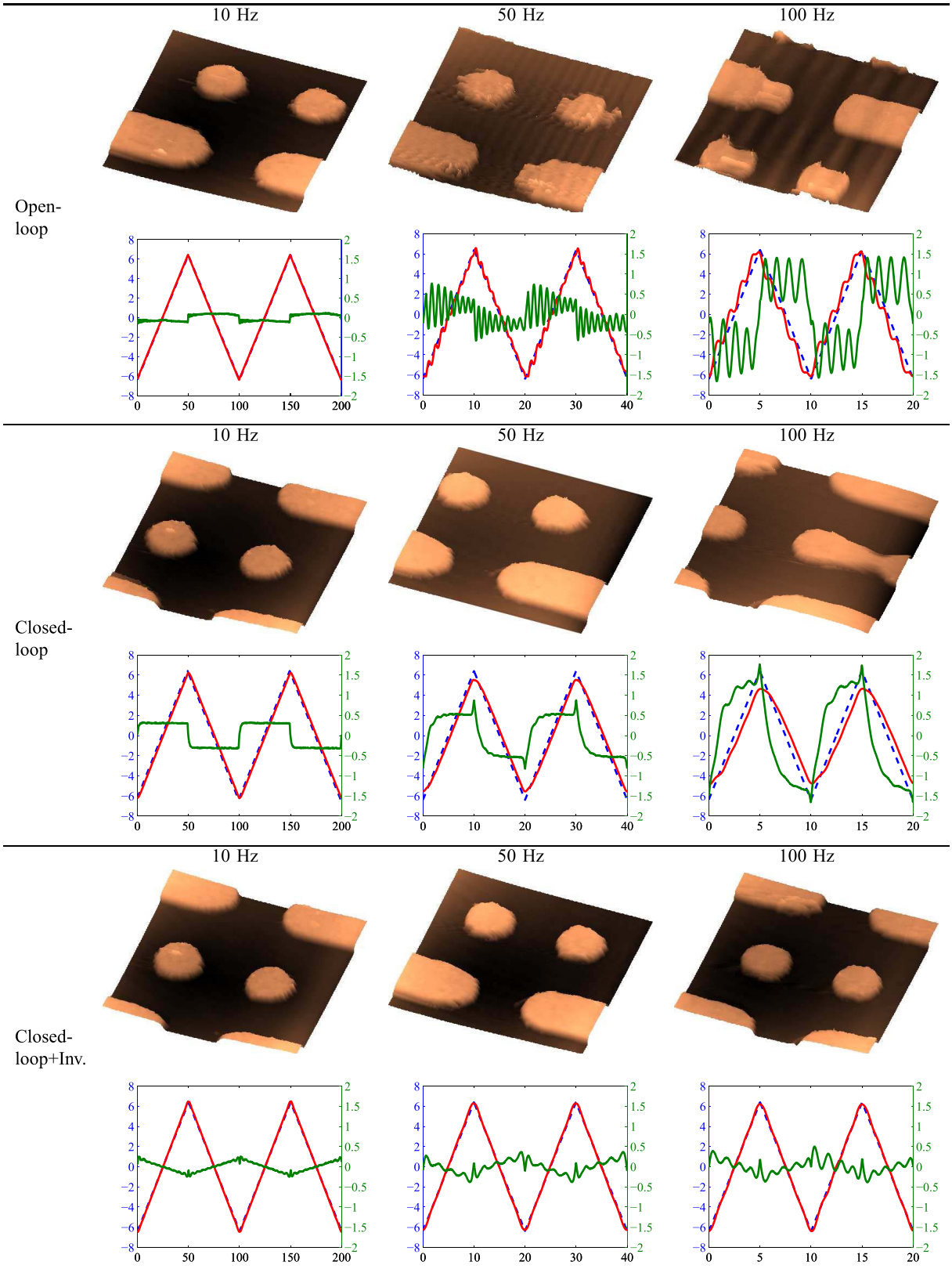

Fig. 12. AFM scan results obtained at 10 Hz, 50 Hz and 100 Hz, in open-loop, closed-loop and closed-loop with inversion feedforward. 3-D topography of the sample is plotted. For the time signal plots, the left-hand scale is for the fast-axis reference (blue) and displacement (red) signals of the nanopositioner. The right-hand scale is for the tracking errors (green). These are plotted in (μm Vs. msec).

The closed-loop frequency responses of the two axes are plotted in Fig. 9. The PPF controller in the damping loop reduces the resonant peak by 22.1 dB. Together with the integral controller with a gain of $K_{ix} = 700$, the achievable closed-loop bandwidth is 165 Hz. The gain and phase margins are 7.24 dB and 80.2°, respectively. For comparison, in a

closed-loop system without the damping loop, but with an integrator, the highest closed-loop bandwidth obtainable is only 16 Hz. The tracking bandwidth is increased tenfold with the implementation of the proposed PPF controller. For the slow axis, where a smaller closed-loop bandwidth is acceptable, the measured bandwidth is 18 Hz with gain and phase margins of 27.2 dB and 87.1° respectively. This bandwidth is sufficient for tracking a slow ramp reference input.

A. Inversion Feedforward

Without feedback control, the highest scan rate achievable on a nanopositioner with a resonance frequency of 860 Hz is 8.6 Hz [1]. Here, the objective is to obtain AFM images with raster scan rates up to 100 Hz. The obtained closed-loop tracking bandwidth of 165 Hz is insufficient to track a fast 100-Hz triangular waveform. Therefore, the inversion-based feedforward technique was used to further increase the tracking bandwidth. A model-based feedforward technique may not be able to compensate for plant uncertainties [35]. However, plant uncertainties can be minimized by means of feedback control [17], [36], [37], i.e. by implementing the two feedback control loops as presented in Sec. V. A model $G_{cl}(s)$ was fitted to the closed-loop frequency response data of the x axis for inversion, see Fig. 10(a). In order to obtain an accurate inversed model $G_{cl}^{-1}(s)$, the frequency range of the model was restricted to 1.5 kHz to reduce modeling errors due to uncertainties in the measured closed-loop data. The inversion feedforward inputs $\hat{r}_x$ were obtained by using all odd harmonics of the triangular waveform that lie within the bandwidth of 1.5 kHz, where the amplitude of the harmonics was scaled by $\mid G_{cl}^{-1}(i\omega) \mid$, and the phase of the harmonics was shifted by $\angle G_{cl}^{-1}(i\omega)$. Note that $\hat{r}_x$ were obtained offline as shown in Fig. 10(a). By implementing the inversion feedforward technique, the tracking bandwidth of the system was increased from 165 Hz to 1.5 kHz.

VI. AFM Imaging Performance

This section reports the AFM images obtained with the feedback controlled MEMS nanopositioner. The experimental setup consisting of the MEMS scanner mounted on a printed circuit board, together with the readout circuitry and a Nanosurf EasyScan 2 AFM, is illustrated in Fig. 11. The experiments were performed in the scan-by-sample mode where the scan table, which is deposited with calibration features (see Fig. 2), was moved in relation to the static probe. The z scanner of the commercial AFM and its in-built vertical feedback controller were activated during the "landing" process to regulate the probe-sample force. After successfully "landing" the probe, the vertical feedback controller was turned off. The MEMS nanopositioner was driven in a raster pattern during the scans. This scanning mode is known as the constant-height contact-mode.

A cantilever probe with a resonance frequency of 13 kHz and a stiffness of 0.2 N/m was used during the scans. The height of the features is approximately 550 nm. The remaining dimensions can be found in Fig. 2. An image area of 12.7 μm × 12.7 μm was scanned at 10 Hz, 50 Hz and 100 Hz in open-loop, closed-loop and closed-loop with inversion. Fig. 12 plots the 3-dimensional topography images, the fast x axis displacements and tracking errors of the nanopositioner.

TABLE I

Maximum and RMS Tracking Error (nm) Obtained in Open-Loop, Closed-Loop and Closed-Loop with Inversion for 90% of the Scan Range

Scan freq.	OL		CL		CL. + Inver.	
(Hz)	Max.	RMS	Max.	RMS	Max.	RMS
10	119.6	87.6	328.4	308.0	215.2	108.4
50	766.7	313.8	541.8	463.8	366.4	166.5
100	1435.2	965.4	1379.4	1018.8	500.4	167.5

At 10 Hz, vibrations are not noticeable in any of the scans. While vibration-induced artefacts appear in the open-loop scans at 50 Hz and 100 Hz, these vibrations are suppressed in closed-loop. However, the associated tracking errors are relatively large which can be seen from the time signal plots in Fig. 12. This is due to the inadequate closed-loop tracking bandwidth of the fast axis, which is only 165 Hz. Image artefacts due to poor tracking can be observed in the 100-Hz closed-loop scans where the round features are smudged and elongated. With the implementation of the inversion feedforward technique, these artefacts are eliminated in the 100 Hz scan which improves the image quality substantially. Table I shows the maximum and RMS tracking errors for 90% of the scan range. With the inversion feedforward technique and the feedback control loops combined, the tracking errors of the 50 Hz and 100 Hz triangular references are significantly reduced by a factor of 1.8 and 8.2 respectively compared to their open-loop counterparts.

VII. Conclusion

Electrothermal displacement sensors were integrated in a 2-DOF electrostatically-actuated nanopositioner on a SOI MEMS chip. The stage, which functions as the scan table, has an area of 3 mm × 3 mm, and a maximum displacement of 16 μm in both the x and y directions. The electrothermal sensor outputs are measured by a transimpedance amplifier circuit, with this output being utilized as a measurement by a controller in a feedback loop. The frequency response and static nonlinearity of the device were characterized in order to implement the controller. The comparison of the scan results obtained by the AFM in open-loop, closed-loop and closed-loop with inversion configurations demonstrate the effectiveness of MEMS-based sensor integration in achieving high-quality AFM scans at high scan speeds.

The successful demonstration of a feedback controlled MEMS nanopositioner to generate images through an AFM scan represents an important step towards the development of a complete miniaturized AFM. Through further work to shrink the remaining components of the system, the ultimate goal of developing a system for true on-chip AFM scanning may be realized.

ACKNOWLEDGMENT

The research was performed in the Laboratory for Dynamics and Control of Nanosystems at The University of Newcastle. The authors would like to acknowledge the support of the Australian Research Council. Some of the SEM images were obtained with the assistance of the Electron Microscope and X-Ray Unit of the University of Newcastle.

REFERENCES

[1] S. Devasia, E. Eleftheriou, and S. O. R. Moheimani, "A survey of control issues in nanopositioning," *IEEE Trans. Control Syst. Technol.*, vol. 15, no. 5, pp. 802–823, Sep. 2007.

[2] J. Shi, J. Dertouzos, A. Gafni, and D. Steel, "Application of single-molecule spectroscopy in studying enzyme kinetics and mechanism," in *Fluorescence Spectroscopy* (Methods in Enzymology), vol. 450, L. Brand and M. L. Johnson, Eds. New York, NY, USA: Academic, 2008, pp. 129–157.

[3] J. J. Gorman, Y. S. Kim, A. E. Vladár, and N. G. Dagalakis, "Design of an on-chip microscale nanoassembly system," *Int. J. Control*, vol. 1, no. 6, pp. 710–721, 2007.

[4] J. J. Gorman, N. G. Dagalakis, and B. G. Boone, "Multi-loop control of a nanopositioning mechanism for ultra-precision beam steering," *Proc. SPIE*, vol. 5160, pp. 170–181, Aug. 2003.

[5] S. Bergna, J. Gorman, and N. Dagalakis, "Design and modeling of thermally actuated MEMS nanopositioners," in *Proc. ASME IMECE*, 2005, pp. 561–568.

[6] J. J. Gorman, Y. S. Kim, and N. G. Dagalakis, "Control of MEMS nanopositioners with nano-scale resolution," in *Proc. ASME IMECE*, Nov. 2006, pp. 1–9.

[7] D. Brouwer, B. de Jong, and H. Soemers, "Design and modeling of a six DOFs MEMS-based precision manipulator," *Precis. Eng.*, vol. 34, no. 2, pp. 307–319, Apr. 2010.

[8] G. Brown, L. Li, R. Bauer, J. Liu, and D. Uttamchandani, "A two-axis hybrid MEMS scanner incorporating electrothermal and electrostatic actuators," in *Proc. Int. Conf. Opt. MEMS Nanophoton.*, Aug. 2010, pp. 115–116.

[9] Y. Zhu, A. Bazaei, S. O. R. Moheimani, and M. R. Yuce, "Design, modeling, and control of a micromachined nanopositioner with integrated electrothermal actuation and sensing," *J. Microelectromech. Syst.*, vol. 20, no. 3, pp. 711–719, Jun. 2011.

[10] M. A. Lantz, H. E. Rothuizen, U. Drechsler, W. Haberle, and M. Despont, "A vibration resistant nanopositioner for mobile parallel-probe storage applications," *J. Microelectromech. Syst.*, vol. 16, no. 1, pp. 130–139, Feb. 2007.

[11] A. Pantazi, A. Sebastian, G. Cherubini, M. Lantz, H. Pozidis, H. Rothuizen, *et al.*, "Control of MEMS-based scanning-probe data-storage devices," *IEEE Trans. Control Syst. Technol.*, vol. 15, no. 5, pp. 824–841, Sep. 2007.

[12] J. Engelen, M. Lantz, H. Rothuizen, L. Abelmann, and M. Elwenspoek, "Improved performance of large stroke comb-drive actuators by using a stepped finger shape," in *Proc. Int. Solid-State Sensors, Actuat. Microsyst. Conf.*, Jun. 2009, pp. 1762–1765.

[13] B. Koo, X. Zhang, J. Dong, S. M. Salapaka, and P. M. Ferreira, "A 2 degree-of-freedom SOI-MEMS translation stage with closed-loop positioning," *J. Microelectromech. Syst.*, vol. 21, no. 1, pp. 13–22, Feb. 2012.

[14] J. Ouyang and Y. Zhu, "Z-shaped MEMS thermal actuators: Piezoresistive self-sensing and preliminary results for feedback control," *J. Microelectromech. Syst.*, vol. 21, no. 3, pp. 596–604, Jun. 2012.

[15] G. Binnig, C. F. Quate, and C. Gerber, "Atomic force microscope," *Phys. Rev. Lett.*, vol. 56, no. 9, pp. 930–933, 1986.

[16] A. G. Fowler, A. N. Laskovski, A. C. Hammond, and S. O. R. Moheimani, "A 2-DOF electrostatically actuated MEMS nanopositioner for on-chip AFM," *J. Microelectromech. Syst.*, vol. 21, no. 4, pp. 771–773, Aug. 2012.

[17] Y. K. Yong, S. O. R. Moheimani, B. J. Kenton, and K. K. Leang, "Invited review article: High-speed flexure-guided nanopositioning: Mechanical design and control issues," *Rev. Sci. Instrum.*, vol. 83, no. 12, pp. 121101-1–121101-22, 2012.

[18] A. Cowen, G. Hames, D. Monk, S. Wilcenski, and B. Hardy, *SOI-MUMPs Design Handbook*. Durham, NC, USA: MEMSCAP Inc., 2011.

[19] L. Ji, Y. Zhu, S. O. R. Moheimani, and M. R. Yuce, "A micromachined 2 DOF nanopositioner with integrated capacitive displacement sensor," in *Proc. IEEE Sensors*, Nov. 2010, pp. 1464–1467.

[20] R. Messenger, Q. Aten, T. McLain, and L. Howell, "Piezoresistive feedback control of a MEMS thermal actuator," *J. Microelectromech. Syst.*, vol. 18, no. 6, pp. 1267–1278, Dec. 2009.

[21] M. A. Lantz, G. K. Binnig, M. Despont, and U. Drechsler, "A micromechanical thermal displacement sensor with nanometer resolution," *Scientific*, vol. 16, no. 8, pp. 1089–1094, 2005.

[22] A. Barlian, W.-T. Park, J. Mallon, A. Rastegar, and B. Pruitt, "Review: Semiconductor piezoresistance for microsystems," *Proc. IEEE*, vol. 97, no. 3, pp. 513–552, Mar. 2009.

[23] B. Krijnen, R. P. Hogervorst, J. W. van Dijk, J. B. C. Engelen, L. A. Woldering, D. M. Brouwer, *et al.*, "A single-mask thermal displacement sensor in MEMS," *J. Micromech. Microeng.*, vol. 21, no. 7, pp. 74007–074018, 2011.

[24] A. G. Fowler, A. Bazaei, and S. O. R. Moheimani, "Design and analysis of nonuniformly shaped heaters for improved MEMS-based electrothermal displacement sensing," *J. Microelectromech. Syst.*, vol. 22, no. 3, pp. 687–694, Jun. 2013.

[25] Y. Zhu, S. O. R. Moheimani, and M. R. Yuce, "Simultaneous capacitive and electrothermal position sensing in a micromachined nanopositioner," *IEEE Electron Device Lett.*, vol. 32, no. 8, pp. 1146–1148, Aug. 2011.

[26] K. Blake, "An990: Analog sensor conditioning circuits—An overview," Microchip Technology Inc., Chandler, AZ, USA, Tech. Rep., 2005.

[27] J. Lu, M. Inerowicz, S. Joo, J. K. Kwon, and B. Jung, "A low-power, wide-dynamic-range semi-digital universal sensor readout circuit using pulsewidth modulation," *IEEE Sensors J.*, vol. 11, no. 5, pp. 1134–1144, May 2011.

[28] A. Mohammadi, M. R. Yuce, and S. O. R. Moheimani, "Frequency modulation technique for MEMS resistive sensing," *IEEE Sensors J.*, vol. 12, no. 8, pp. 2690–2698, Aug. 2012.

[29] T. McKelvey, H. Akcay, and L. Ljung, "Subspace based multivariable system identification from frequency response data," *IEEE Trans. Autom. Control*, vol. 41, no. 7, pp. 960–978, Jul. 1996.

[30] C. J. Goh and T. K. Caughey, "On the stability problem caused by finite actuator dynamics in the collocated control of large space structures," *Int. J. Control*, vol. 41, no. 3, pp. 787–802, 1985.

[31] J. L. Fanson and T. K. Caughey, "Positive position feedback control for large space structures," *AIAA J.*, vol. 28, no. 4, pp. 717–724, 1990.

[32] S. O. R. Moheimani, B. J. G. Vautier, and B. Bhikkaji, "Experimental implementation of extended multivariable PPF control on an active structure," *IEEE Trans. Control Syst. Technol.*, vol. 14, no. 3, pp. 443–455, May 2006.

[33] I. A. Mahmood and S. O. R. Moheimani, "Making a commercial AFM more accurate and faster using positive position feedback control," *Rev. Sci. Instrum.*, vol. 80, no. 6, pp. 063705-1–063705-8, 2009.

[34] K. K. Leang and S. Devasia, "Feedforward control of piezoactuators in atomic force microscope systems: Inversion-based compensation for dynamics and hysteresis," *IEEE Trans. Control Syst. Technol.*, vol. 15, no. 5, pp. 927–935, Sep. 2007.

[35] Y. Zhao and S. Jayasuriya, "Feedforward controllers and tracking accuracy in the presence of plant uncertainty," *ASME J. Dyn. Syst., Meas., Control*, vol. 117, no. 4, pp. 490–495, 1995.

[36] S. S. Aphale, S. Devasia, and S. O. R. Moheimani, "High-bandwidth control of a piezoelectric nanopositioning stage in the present of plant uncertainties," *Nanotechnology*, vol. 19, no. 12, pp. 125503-1–125503-9, 2008.

[37] K. K. Leang, Q. Zou, and S. Devasia, "Feedforward control of piezoactuators in atomic force microscope systems: Inversion-based compensation for dynamics and hysteresis," *IEEE Control Syst. Mag.*, vol. 29, no. 1, pp. 70–82, Feb. 2009.

Ali Mohammadi (S'09) received the B.Sc. and M.Sc. degrees in electrical and electronics engineering from Urmia University, Urmia, Iran, and the Iran University of Science and Technology, Tehran, Iran, in 2003 and 2007, respectively. He is currently pursuing the Ph.D. degree with the University of Newcastle, Australia where he has been awarded an Endeavour International Postgraduate Research Scholarship. His previous research involves data-converters and frequency synthesizers for telecommunication systems. His current research interests include MEMS sensors with special focus on the interface circuit design.

Anthony G. Fowler (S'10) was born in Taree, Australia. He received the Bachelor's degree in electrical engineering from The University of Newcastle, Callaghan, Australia, in 2010. He is the recipient of an Australian Postgraduate Award, and is currently pursuing the Ph.D. degree in electrical engineering at the same university.

His research interests include the design and analysis of novel MEMS devices for energy harvesting and nanopositioning applications.

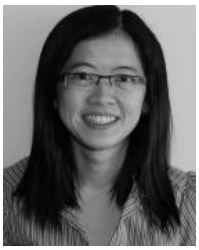

Yuen K. Yong (M'09) received the B.Eng. degree (1st Class Honors) in mechatronic engineering and the Ph.D. degree in mechanical engineering from The University of Adelaide, Adelaide, Australia, in 2001 and 2007, respectively. She is currently an Australian Research Council DECRA Fellow with the School of Electrical Engineering and Computer Science, The University of Newcastle. Her research interests include the design and control of nanopositioning systems, high-speed atomic force microscopy, finite-element analysis of smart materials and structures, and sensing and actuation.

Dr. Yong was a recipient of the 2008 IEEE/ASME International Conference on Advanced Intelligent Mechatronics (AIM) Best Conference Paper Finalist Award. She is a member of the Technical Program Committee of AIM and the International Conference on Manipulation, Manufacturing, and Measurement on the Nanoscale (3M-NANO). She is also an associate editor of the *International Journal of Advanced Robotic Systems*.

S. O. Reza Moheimani (F'11) received his undergraduate degree in electrical engineering from Shiraz University in 1991 and completed his doctoral studies at the University of New South Wales, Australia, in 1996. In 1997 he joined The University of Newcastle, Australia, embarking on a new research program addressing the dynamics and control design issues related to high-precision mechatronic systems. Professor Moheimani is the founder and director of the Laboratory for Dynamics and Control of Nanosystems, a multimillion-dollar state-of-the-art research facility. His current research interests are mainly in the area of ultrahigh-precision mechatronic systems, with particular emphasis on dynamics and control at the nanometer scale, including applications of control and estimation in nanopositioning systems for high-speed scanning probe microscopy, modeling and control of microcantilever-based devices, control of microactuators in microelectromechanical systems, and design, modelling and control of micromachined nanopositioners for on-chip atomic force microscopy.

His work has been recognised by a number of awards including the IFAC Nathaniel B. Nichols Medal (2014); IFAC Mechatronic Systems Award (2013); IEEE Control Systems Technology Award (2009); Australian Research Council Future Fellowship (2009); IEEE TRANSACTIONS ON CONTROL SYSTEMS TECHNOLOGY Outstanding Paper Award (2007); Australian Research Council Postdoctoral Fellowship (1999); and several best student paper awards in various conferences. He has served on the editorial boards of a number of journals, including the IEEE/ASME TRANSACTIONS ON MECHATRONICS, IEEE TRANSACTIONS ON CONTROL SYSTEMS TECHNOLOGY, and *Control Engineering Practice*. He has chaired several international conferences and workshops and currently chairs the IFAC Technical Committee on Mechatronic Systems. He has published over 270 refereed papers and five books and edited volumes. He is a Fellow of IEEE, IFAC and Institute of Physics (UK).